

Real-time detection of voltage patterns in the brain

Tomas Fiers

Thesis submitted for the degree of
Master of Science in
Biomedical Engineering

Thesis supervisors:

Prof. dr. ir. A. Bertrand
Prof. dr. F. Kloosterman

Assessors:

Prof. dr. ir. R. Puers
Dr. eng. J. Couto

Mentors:

Ir. J. Wouters
Dott. D. Ciliberti

© Copyright KU Leuven

Without written permission of the thesis supervisors and the author it is forbidden to reproduce or adapt in any form or by any means any part of this publication. Requests for obtaining the right to reproduce or utilize parts of this publication should be addressed to Faculteit Ingenieurswetenschappen, Kasteelpark Arenberg 1 bus 2200, B-3001 Heverlee, +32-16-321350.

A written permission of the thesis supervisors is also required to use the methods, products, schematics and programmes described in this work for industrial or commercial use, and for submitting this publication in scientific contests.

Abstract – 30 Nov

Contents

Abbreviations	6
Symbols	7
1 Introduction – 16 Nov [9p]	9
1.1 Closed-loop brain-computer interfaces [1p]	9
1.2 Sharp wave-ripples [6p]	9
1.3 Problem statement [1p]	9
1.4 Thesis overview [1p]	9
2 Single-channel linear filtering – 2 Nov [10p]	10
2.1 Offline labelling of SWR segments [3p]	10
2.2 State of the art online SWR detectors [3p]	10
2.3 Quantifying & comparing detectors [4p]	10
3 Multi-channel linear filtering – 26 Oct [10p]	11
3.1 Data-driven algorithms [1p]	11
3.2 Linear signal-to-noise maximisation [2p]	11
3.3 Result for SWR detection	14
3.4 Combining space and time [1p]	17
3.5 Regularization [1p]	17
3.6 Channels [1p]	17
3.7 Delays [1p]	17
3.8 Multiple eigenvectors [2p]	17
3.9 Spectral preprocessing [1p]	17
4 Nonlinear signal detection – 9 Nov [9p]	18
4.1 Recurrent neural networks [2p]	18
4.2 Optimization [3p]	18
4.3 Regularization [2p]	18
4.4 Channels [1p]	18
4.5 Network size [1p]	18
5 Discussion – 23 Nov [4p]	19
5.1 Comparing detectors [2p]	19
5.2 Further work [2p]	19

<i>CONTENTS</i>	5
6 Conclusions – 30 Nov [1p]	20
References	21
Appendices	22

Abbreviations

BPF	Band-pass filter. See chapter 2.
CA1	“Cornu Ammonis”, subregion 1. Region in the hippocampus where voltages are recorded from (see ???).
CA3	“Cornu Ammonis”, subregion 3. Region in the hippocampus (see ???). CA3 sends many axons (called “Schafer collaterals”) to CA1.
IQR	Interquartile range. A measure of the spread of a set of one-dimensional values, that is robust to outliers. Difference between the 75th and the 25th data percentile.
GEVec	Generalized eigenvector. See section 3.2.
GEVal	Generalized eigenvalue. See section 3.2.
LFP	Local field potential. The extracellular electric potential (see ??).
RMS	Root-mean-square. $\sqrt{\langle x_t^2 \rangle}$ for a signal x_t .
RNN	Recurrent neural network. See chapter 4.
SWR	Sharp wave-ripple. The pattern in the LFP that we want to detect in real-time. See ??.
SNR	Signal-to-noise ratio. See section 3.2.
SOTA	State of the art. The algorithm currently used for SWR detection, namely an online single channel band-pass filter.

Symbols

Notation

- y Scalars are denoted in lowercase italic.
- \mathbf{z} Vectors are denoted in lowercase boldface.
- \mathbf{A} Matrices are denoted in uppercase boldface.
- $\langle \cdot \rangle$ Time-average of a signal.
- \odot Elementwise multiplication. (“Hadamard product”).
- $\sigma(\cdot)$ Sigmoid ‘squashing’ function. $\sigma(x) = \frac{1}{1+\exp(-x)}$, $\in (0, 1)$.
- $\tanh(\cdot)$ Hyperbolic tangent. $\tanh(x) = 2 \sigma(x) - 1$, $\in (-1, 1)$.

Signals

- \mathbf{z}_t Digitized LFP sample at discrete time step t . $\mathbf{z}_t \in \mathbb{R}^C$, with C the number of channels (i.e. the number of electrodes simultaneously recorded from). Input to an SWR detection algorithm.
- o_t Output signal of an SWR detection algorithm, $\in \mathbb{R}$.
- n_t ‘Envelope’. Transformation of o_t , so that it is constrained to \mathbb{R}^+ . Should be high when the corresponding input sample \mathbf{z}_t is part of an SWR segment, and low when it is not. $n_t = |o_t|$ for online linear filters; $n_t = \sigma(o_t)$ for the RNN’s of chapter 4.
- y_t Binary target signal, used when training data-driven SWR detection algorithms. We define $y_t = 1$ when the corresponding input sample \mathbf{z}_t is part of an SWR segment, and $y_t = 0$ when it is not.

Measures & parameters

- P Precision. Also known as positive predictive value. The fraction of correct detections versus all detections.
- R Recall. Also known as sensitivity, hit rate, or true positive rate. The fraction of detected reference SWR segments versus all reference SWR segments.
- F_β F-score: weighted harmonic mean of recall and precision. $F_\beta = \frac{(1+\beta^2)PR}{\beta^2 P + R}$. Measures detection performance “for a user who attaches β times as much importance to recall as to precision.” [1]
- F_1 F-score where recall and precision are weighted equally. For the common case where the PR -curve is concave, $F_1(T)$ is maximal when $P(T) = R(T)$ ($= F_1(T)$).
- T Detection threshold applied to the envelope n_t , $T \in (\min n_t, \max n_t)$. Each threshold T yields a different P -value, R -value, F_1 -value, etc.

Introduction – 16 Nov [9p]

1.1 Closed-loop brain-computer interfaces [1p]

1.2 Sharp wave-ripples [6p]

Description [2p]

Scientific importance [2p]

Biophysics [1p]

Closed-loop technology [1p]

1.3 Problem statement [1p]

1.4 Thesis overview [1p]

Chapter 2

Single-channel linear filtering – 2

Nov [10p]

- 2.1 Offline labelling of SWR segments [3p]
- 2.2 State of the art online SWR detectors [3p]
- 2.3 Quantifying & comparing detectors [4p]

Multi-channel linear filtering – 26 Oct [10p]

3.1 Data-driven algorithms [1p]

In this and the following chapter, we describe *supervised*, or data-driven SWR detection algorithms: they require training data $\mathbf{z}_t^{\text{train}}$, and an associated labelling y_t^{train} which marks the presence of an SWR event in $\mathbf{z}_t^{\text{train}}$, for every discrete time sample t . We arbitrarily define $y_t \in \{0, 1\}$, with $y_t = 1$ when the corresponding input sample \mathbf{z}_t is part of an SWR segment, and $y_t = 0$ when it is not.

The problem of obtaining such a labelling y_t for some recording data \mathbf{z}_t is the topic of section 2.1. Training labels can be obtained either by human expert labellers, or by using an automated *offline* SWR detection algorithm, where we assume that the automated labelling corresponds well to a supposed human expert labelling. In this thesis, we use the automated labelling method of section 2.1 to generate target labellings y_t^{train} .

Before a supervised algorithm can be used for real-time detection, its parameters have to be ‘tuned’. This is done using a training dataset $(\mathbf{z}_t^{\text{train}}, y_t^{\text{train}})$, during the so called *training phase*. Parameters are changed such that the algorithm’s output o_t for an input $\mathbf{z}_t^{\text{train}}$ matches the target labelling y_t^{train} well. Sections 3.2 and 4.2 describe how this tuning can be done for two concrete detection algorithms.

The hope is that the trained algorithm also performs well on input data $\mathbf{z}_t^{\text{test}}$ not part of the training set. That is, that the algorithm has good *generalization performance*. When this is not the case and the algorithm is tuned so that it only performs well on the training data, we say that the algorithm has been *overfit*. Often, so called *regularization* methods exist to discourage overfitting on the training data. Some example regularization methods are discussed in sections 3.5 and 4.3.

3.2 Linear signal-to-noise maximisation [2p]

In this chapter, we search for a linear combination of channels that yields an output signal o_t useful for sharp wave-ripple detection. More precisely, we search for a vector

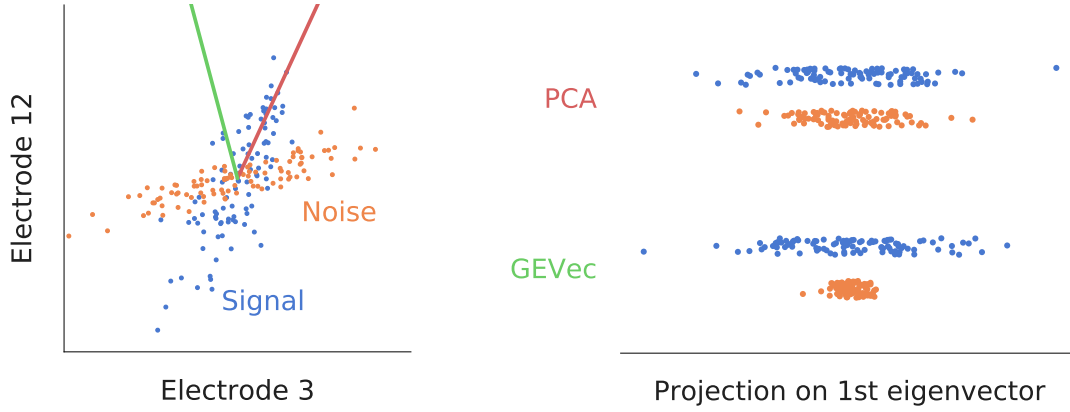


Figure 3.1: **Linear signal-to-noise maximisation.** Toy example to illustrate the generalized eigenvector approach to signal detection. *Left*: multi-channel time-series data plotted in ‘phase space’ (meaning without time axis), with blue dots representing samples where the signal was present, and orange dots representing samples where it was not. Actually toy data drawn from two 2-dimensional Gaussian distributions with different covariance matrices. Red vector: first eigenvector of the signal covariance matrix (also known as the first principal component). Green vector: first generalized eigenvector of the signal and noise covariance matrices. *Right*: Projection of both data sets on both the ordinary eigenvector (“PCA”) and the generalized eigenvector (“GEVec”). The ratio of the projected signal data variance versus the projected noise data variance is maximised for the GEVec case.

$\mathbf{w} \in \mathbb{R}^C$ in channel (or electrode) space to project the samples $\mathbf{z}_t \in \mathbb{R}^C$ on, so that the output signal

$$o_t = \mathbf{w}^T \mathbf{z}_t \quad (3.1)$$

has high variance (or power) during SWR events, and low variance outside them.¹ This principle is illustrated with a two-dimensional toy dataset in fig. 3.1. We can then detect SWR events using threshold crossings of the envelope of o_t , as discussed in section 2.2.

The next two sections describe how this vector \mathbf{w} can be found.

The optimisation problem

Suppose all training samples $\mathbf{z}_t^{\text{train}}$ are gathered and divided over two data matrices $\mathbf{S} \in \mathbb{R}^{C \times N_S}$ and $\mathbf{N} \in \mathbb{R}^{C \times N_N}$, where \mathbf{S} (for ‘signal’) contains all N_S samples of $\mathbf{z}_t^{\text{train}}$ where an SWR is present, and \mathbf{N} (for ‘noise’) contains all N_N other samples. (These matrices can be easily constructed by concatenating segments from $\mathbf{z}_t^{\text{train}}$).

¹We assume that the input signals are zero-mean, such that the power P of the output signal equals its variance: $P_o = \langle o_t^2 \rangle = \langle (o_t - \mu_o)^2 \rangle = \text{Var}(o_t)$ when $\mu_o = 0$, which is the case for zero-mean input channels: $\mu_o = \langle o_t \rangle = \langle \mathbf{w}^T \mathbf{z}_t \rangle = \sum_i w_i \langle z_{t,i} \rangle = 0$ when $\langle z_{t,i} \rangle = 0$ for all channels i .

This zero-mean assumption is reasonably well fulfilled for the analysed recording: the sample values of a 10-second moving average of the recording are near zero (median $-0.02 \mu\text{V}$, IQR $0.13 \mu\text{V}$. In comparison, the RMS-value of the recording is $210 \mu\text{V}$).

Input data that is not zero-mean can be readily transformed to be so (even in an online setting), by subtracting a (moving) average from the input signal.

Equation (3.1) then becomes, in vector notation:

$$\begin{aligned}\mathbf{o}_S &= \mathbf{w}^T \mathbf{S} \\ \mathbf{o}_N &= \mathbf{w}^T \mathbf{N},\end{aligned}$$

where each element of the row vectors \mathbf{o}_S and \mathbf{o}_N is a filtered sample of \mathbf{S} and \mathbf{N} , respectively. Figure 3.1 (right) shows the distribution of the values in two example data vectors \mathbf{o}_S and \mathbf{o}_N .

We want to find the weight vector $\hat{\mathbf{w}}$ that maximises the variance of \mathbf{o}_S versus the variance of \mathbf{o}_N , i.e.

$$\begin{aligned}\hat{\mathbf{w}} &= \arg \max_{\mathbf{w}} \frac{\text{Var}(\mathbf{o}_S)}{\text{Var}(\mathbf{o}_N)} \\ &= \arg \max_{\mathbf{w}} \frac{\frac{1}{N_S} \mathbf{o}_S \mathbf{o}_S^T}{\frac{1}{N_N} \mathbf{o}_N \mathbf{o}_N^T} \\ &= \arg \max_{\mathbf{w}} \frac{\frac{1}{N_S} \mathbf{w}^T \mathbf{S} \mathbf{S}^T \mathbf{w}}{\frac{1}{N_N} \mathbf{w}^T \mathbf{N} \mathbf{N}^T \mathbf{w}}\end{aligned}\tag{3.2}$$

In this last equation, we recognize the empirical covariance matrices \mathbf{R}_{SS} and \mathbf{R}_{NN} , which are defined as:

$$\mathbf{R}_{SS} = \frac{1}{N_S} \mathbf{S} \mathbf{S}^T \tag{3.3}$$

$$\mathbf{R}_{NN} = \frac{1}{N_N} \mathbf{N} \mathbf{N}^T \tag{3.4}$$

$\mathbf{R}_{SS} \in \mathbb{R}^{C \times C}$ and $\mathbf{R}_{NN} \in \mathbb{R}^{C \times C}$ are symmetric matrices, where each diagonal element yields the variance of a channel, and each off-diagonal element yields the covariance between a pair of channels.

The condition for the optimal weight vector, eq. (3.2), is thus equivalent to:

$$\hat{\mathbf{w}} = \arg \max_{\mathbf{w}} \frac{\mathbf{w}^T \mathbf{R}_{SS} \mathbf{w}}{\mathbf{w}^T \mathbf{R}_{NN} \mathbf{w}} \tag{3.5}$$

In appendix B, we show that the solution $\hat{\mathbf{w}}$ to this optimisation problem is the first so called “generalized eigenvector” of $(\mathbf{R}_{SS}, \mathbf{R}_{NN})$.

The generalized eigenproblem

An arbitrarily scaled vector \mathbf{w}_i is a so called *generalized eigenvector* (GEVec) for the ordered matrix pair $(\mathbf{R}_{SS}, \mathbf{R}_{NN})$ when the following holds:

$$\mathbf{R}_{SS} \mathbf{w}_i = \lambda_i \mathbf{R}_{NN} \mathbf{w}_i, \tag{3.6}$$

for some scalar λ_i , which is called the *generalized eigenvalue* (GEVal) corresponding to \mathbf{w}_i . The largest scalar λ_1 for which eq. (3.6) holds is the ‘first’ GEVal, and as mentioned before, the corresponding GEVec \mathbf{w}_1 is the solution $\hat{\mathbf{w}}$ to eq. (3.5).

Since the 1960's, numerically stable algorithms exist that solve the generalised eigenproblem eq. (3.6) [2]. A specialized algorithm is applicable when the input matrices are symmetric – as is the case for \mathbf{R}_{SS} and \mathbf{R}_{NN} . This algorithm (based on a Cholesky factorization and the classical QR-algorithm for ordinary eigenproblems) is implemented in the LAPACK software package (as `ssygv` and `dsygv`), and can be easily accessed using e.g. the `eig` function from MATLAB, or the `eigh` function from SciPy's `linalg` module.

3.3 Result for SWR detection

We divided the 34-minute long LFP recording into two datasets. The first 60% was used as training data, to calculate the covariance matrices \mathbf{R}_{SS} and \mathbf{R}_{NN} , and to calculate from these the optimal linear combination of channels $\hat{\mathbf{w}}$, as described in the preceding sections. The remaining 40% was used to evaluate this filter $\hat{\mathbf{w}}$, and to compare it to the state-of-the-art method (the single-channel online band-pass filter). The 60-40 division was chosen arbitrarily, under the constraint that there are sufficient amounts of both training and test data.

Figure 3.2A shows an excerpt of the test input signal, and the corresponding filter output envelopes (blue for state-of-the art method, orange for GEVec-based multichannel method). Filter outputs o_t are rectified to obtain envelopes $n_t = |o_t|$). Additional excerpts are shown in fig. C.1. The elements of $\hat{\mathbf{w}}$ (i.e. the filter weights) are visualized in fig. 3.2B.

It is clear that the GEVec filter output indeed has high power during SWR events, as promised by the theoretical derivation. The filter weights and signal excerpts reveal that the GEVec output is composed mainly of a few channels in the stratum radiatum (channels 4-5-6 here), where they pick up the sharp waves. However, the filter output envelope is also high for sharp wave-like activity on these channels, without or with only very weak ripple activity in the higher channels: see figs. C.1a, C.1b and C.1d. This results in false positive detections.

We also notice some premature detections (figs. C.1a and C.1c), where the sharp wave – and thus also the GEVec filter output – already has high power before the corresponding ripple has started. The GEVec detection then happens before the start of the reference SWR-segment, which is based on ripple power. These early detections thus count (arguably unfairly so) as false positives, under the evaluation scheme that we use.

This effect, where the sharp wave is discernible before the ripple, results in faster detections when the detection *does* fall within the reference segment. When all 468 SWR events from the test set are analysed, we find a large improvement in detection latency: at thresholds where both methods detect 80% of these reference SWR segments, the median absolute detection latency drops from 24 ms for the state-of-the-art online band-pass filter to 12 ms for the GEVec-based filter. The relative detection latency drops by 32.5 percentage points, from 58.1% to 25.6%. Similar latency improvements are found for other recall and precision values: see fig. 3.3.

This strong improvement in detection latency trades off with an increase in false positives, as was already observed qualitatively. At the aforementioned sensitivity of 80%, the state-of-the-art method has a precision of 94%, whereas the GEVec-based method has

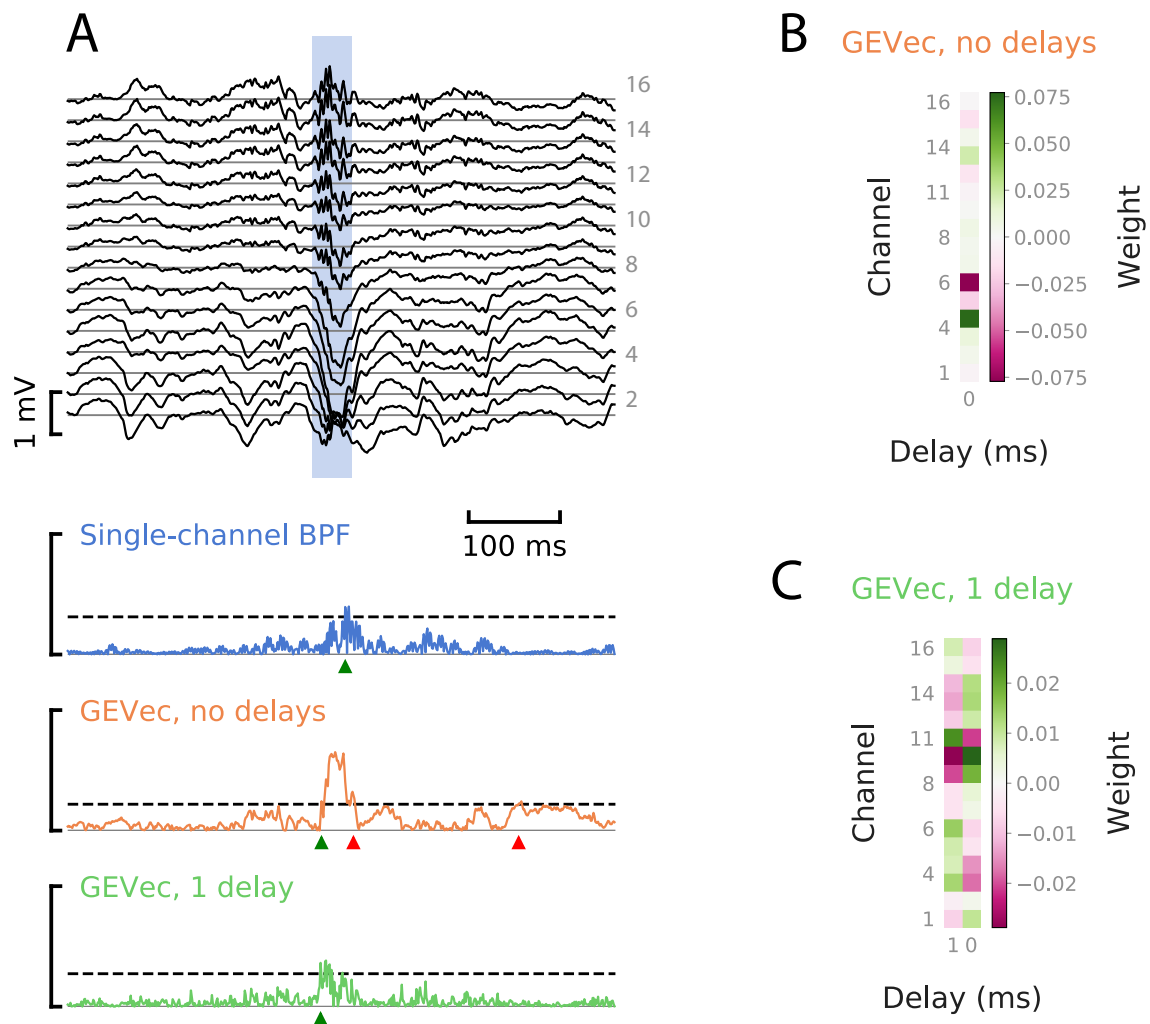


Figure 3.2: **Linear, SNR-maximising combinations of electrodes.**

A. Example input and output signals. *Top*: multi-channel LFP, z_t . Light-blue vertical band: a reference SWR segment. *Bottom*: output envelopes n_t , for different filtering algorithms. Dashed horizontal lines: detection thresholds, chosen so that each algorithm reaches a recall value of 80%. Green triangles: correct detections. Red triangles: incorrect detections. Brackets indicate envelope range (min, max) over the entire test set.

B. Generalised eigenvector \hat{w} (i.e. the weights of the multichannel filter), for a purely spatial filter.

C. Generalised eigenvector \hat{w} for a spatiotemporal filter with a one-sample delay.

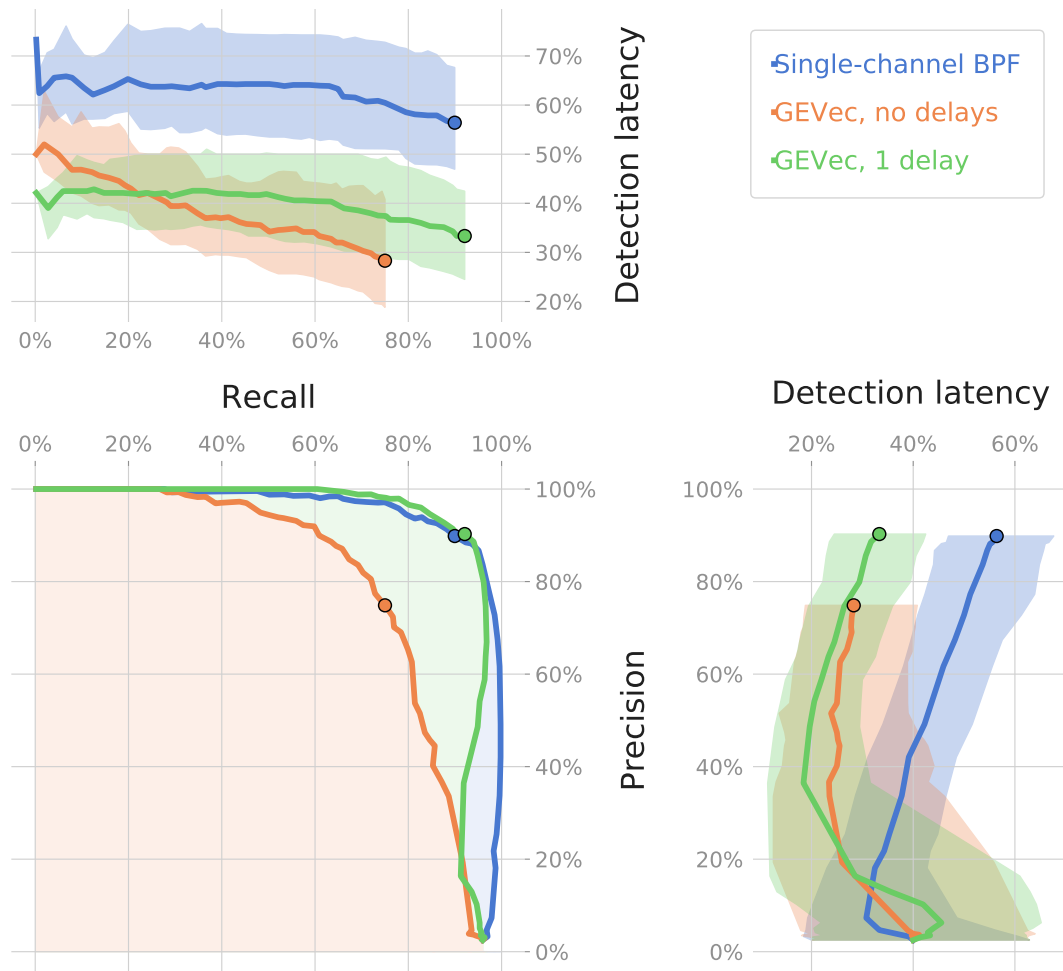


Figure 3.3: **Sensitivity, precision & latency tradeoffs**, for different linear filters & for a range of thresholds.

Each threshold setting for an algorithm corresponds to a point on the precision-recall curve in the bottom-left panel, and to a distribution of relative detection latencies. The median and interquartile range of this distribution are plotted in the top-left or bottom-right panel (as a point of the bold curve, and a slice of the shaded band, respectively).

These latency distribution plots are divided over two panels so that their entire range can be clearly visualized, both for the low recall – high precision regime as for the high recall – low precision regime. The cutoff is made at the point where recall equals precision (AKA the $\max F_1$ point), marked with shaded black circles.

a precision of only 63% (i.e. more than a third of detected events are classified as false positives). This strong decrease in precision is true over the entire PR -curve: see fig. 3.3.

3.4 Combining space and time [1p]

It is hardly surprising that the GEVec-based algorithm as described above cannot discern ripple activity (which is by definition a temporal pattern), as the algorithm is a purely *spatial* filter: at each timestep t , only current information from the different channels is used in calculating the output o_t , without incorporating temporal information from previous timesteps $t_p < t$.

The GEVec method can be easily adapted to also incorporate temporal information however, by defining a vector $\mathbf{z}_t^{\text{stack}} \in \mathbb{R}^{CP}$ which consists of stacked sample vectors (each consisting of C channels) from P different timesteps $t_p \leq t$. The linear weights $\mathbf{w}^{\text{stack}} \in \mathbb{R}^{CP}$ used to obtain the output signal $o_t = (\mathbf{w}^{\text{stack}})^T \mathbf{z}_t^{\text{stack}}$ are then calculated analogously to the purely spatial filter, i.e. as the first generalised eigenvector of the ordered pair $(\mathbf{R}_{SS}^{\text{stack}}, \mathbf{R}_{NN}^{\text{stack}})$, with both covariance matrices $\in \mathbb{R}^{CP \times CP}$.

Adding just one such delayed time step (i.e. $P = 2$) yields a major performance improvement (see fig. 3.3): the precision-recall curve shoots up to (and even slightly exceeds) the PR -curve of the state-of-the-art algorithm, while the latency improvements of the ‘no delay’ GEVec algorithm are mostly retained: at a sensitivity of 80%, the median absolute latency for the one delay GEVec filter is 15 ms, which is 9 ms faster than the state-of-the-art method (and 3 ms slower than the no delay GEVec filter). The relative latency is 36.6%: 21.5 percentage-points lower than the state-of-the-art (and 11 pp. higher than the no delay GEVec filter).

At this 80% recall mark, the one delay GEVec filter attains a precision of 97%, a 3% increase over the state-of-the-art. The full precision-recall-latency tradeoff and algorithm comparison is shown in fig. 3.3. Note that for very low thresholds, the PR -curve of the one-delay GEVec method is no longer concave: decreasing the threshold further yields more (not less) missed reference SWR segments. Figure 3.2C shows the GEVec $\mathbf{w}^{\text{stack}}$. Figure 3.2A and fig. C.1 show example output envelopes (green traces).

These results, particularly the visualized weights in fig. 3.2C, indicate that this one-delay GEVec filter utilizes spatiotemporal information about both the sharp wave and the ripple.

3.5 Regularization [1p]

3.6 Channels [1p]

3.7 Delays [1p]

3.8 Multiple eigenvectors [2p]

3.9 Spectral preprocessing [1p]

Nonlinear signal detection – 9 Nov [9p]

- 4.1 Recurrent neural networks [2p]
- 4.2 Optimization [3p]
- 4.3 Regularization [2p]
- 4.4 Channels [1p]
- 4.5 Network size [1p]

Discussion – 23 Nov [4p]

5.1 Comparing detectors [2p]

5.2 Further work [2p]

Conclusions – 30 Nov [1p]

References

- [1] C. J. Van Rijsbergen. *Information Retrieval*. 2nd. Newton, MA, USA: Butterworth-Heinemann, 1979. URL: <http://www.dcs.gla.ac.uk/Keith/Preface.html>.
- [2] Gene H. Golub and Charles F. Van Loan. *Matrix Computations*. Fourth edition. The Johns Hopkins University Press, 2013.
- [3] Lloyd N. Trefethen and David III Bau. *Numerical Linear Algebra*. Siam, 1997.

Appendices

A	Data description	23
B	Generalized eigenvectors maximise signal-to-noise	24
	Theorem	24
	Proof	24
C	Supplemental figures	27

Appendix A

Data description

Appendix B

Generalized eigenvectors maximise signal-to-noise

In this appendix we show that the solution $\hat{\mathbf{w}}$ to eq. (3.5) is equivalent to the first generalised eigenvector \mathbf{w}_1 of the ordered symmetric, matrix pair $(\mathbf{R}_{SS}, \mathbf{R}_{NN})$ (as defined in section 3.2).

Equation (3.5) is a quotient of quadratic forms, namely the so called “generalized Rayleigh quotient” of $(\mathbf{R}_{SS}, \mathbf{R}_{NN})$. In the following, we denote this matrix pair with (\mathbf{A}, \mathbf{B}) , for lighter notation.

The generalized Rayleigh quotient of a non-zero vector $\mathbf{w} \in \mathbb{R}^N$ and the ordered matrix pair (\mathbf{A}, \mathbf{B}) is thus the scalar $r(\mathbf{w})$ defined as:

$$r(\mathbf{w}) = \frac{\mathbf{w}^T \mathbf{A} \mathbf{w}}{\mathbf{w}^T \mathbf{B} \mathbf{w}} \quad (\text{B.1})$$

We must then prove the following:

Theorem

The first generalised eigenvector \mathbf{w}_1 of (\mathbf{A}, \mathbf{B}) , which corresponds to the largest generalised eigenvalue λ_1 , is also the vector $\hat{\mathbf{w}}$ that maximises the generalized Rayleigh quotient $r(\mathbf{w})$

Proof

As a first step, we will show that if $\hat{\mathbf{w}}$ is the maximum of $r(\mathbf{w})$, that it is indeed an eigenvector of (\mathbf{A}, \mathbf{B}) . In the second step, we will show that the largest eigenvalue λ_1 of (\mathbf{A}, \mathbf{B}) corresponds to the maximum of $r(\mathbf{w})$.

If $\hat{\mathbf{w}}$ is a maximum of $r(\mathbf{w})$, then

$$\nabla r(\hat{\mathbf{w}}) = \mathbf{0}. \quad (\text{B.2})$$

Working out the partial derivatives that comprise the gradient of $r(\mathbf{w})$, we find:

$$\nabla r(\mathbf{w}) = \frac{2\mathbf{A}\mathbf{w}(\mathbf{w}^T\mathbf{B}\mathbf{w}) - 2\mathbf{B}\mathbf{w}(\mathbf{w}^T\mathbf{A}\mathbf{w})}{(\mathbf{w}^T\mathbf{B}\mathbf{w})^2}$$

With eq. (B.2), we then have the following condition for our maximising vector $\hat{\mathbf{w}}$:

$$2\mathbf{A}\hat{\mathbf{w}}(\hat{\mathbf{w}}^T\mathbf{B}\hat{\mathbf{w}}) = 2\mathbf{B}\hat{\mathbf{w}}(\hat{\mathbf{w}}^T\mathbf{A}\hat{\mathbf{w}})$$

or

$$\mathbf{A}\hat{\mathbf{w}} = \frac{\hat{\mathbf{w}}^T\mathbf{A}\hat{\mathbf{w}}}{\hat{\mathbf{w}}^T\mathbf{B}\hat{\mathbf{w}}} \mathbf{B}\hat{\mathbf{w}}$$

$$\mathbf{A}\hat{\mathbf{w}} = r(\hat{\mathbf{w}}) \mathbf{B}\hat{\mathbf{w}}$$

This is the generalised eigenvalue/eigenvector definition (eq. (3.6)) for $\mathbf{w}_i = \hat{\mathbf{w}}$ and $\lambda_i = r(\hat{\mathbf{w}})$.

We have thus shown that if $\hat{\mathbf{w}}$ is a maximum of $r(\mathbf{w})$, that it is an eigenvector of (\mathbf{A}, \mathbf{B}) , with $r(\hat{\mathbf{w}})$ its corresponding eigenvalue.

As the second step, we now show that $r(\hat{\mathbf{w}})$ is the *largest* eigenvalue of (\mathbf{A}, \mathbf{B}) . We follow the reasoning of [3, p. 204], who prove a related result for the ordinary Rayleigh quotient.

We will rewrite the generalised Rayleigh quotient $r(\mathbf{w})$ by writing the arbitrary vector \mathbf{w} as a linear combination of the generalised eigenvectors \mathbf{w}_i of (\mathbf{A}, \mathbf{B}) : $\mathbf{w} = \sum_i c_i \mathbf{w}_i$. Then:

$$\begin{aligned} r(\mathbf{w}) &= \frac{(\sum_i c_i \mathbf{w}_i)^T \mathbf{A} (\sum_i c_i \mathbf{w}_i)}{(\sum_i c_i \mathbf{w}_i)^T \mathbf{B} (\sum_i c_i \mathbf{w}_i)} \\ &= \frac{\sum_i c_i^2 \mathbf{w}_i^T \mathbf{A} \mathbf{w}_i}{\sum_i c_i^2 \mathbf{w}_i^T \mathbf{B} \mathbf{w}_i} \\ &= \frac{\sum_i c_i^2 \lambda_i \mathbf{w}_i^T \mathbf{B} \mathbf{w}_i}{\sum_i c_i^2 \mathbf{w}_i^T \mathbf{B} \mathbf{w}_i} \end{aligned}$$

Generalised eigenvectors are defined up to a scaling factor. We may therefore define our \mathbf{w}_i to be scaled such that $\mathbf{w}_i^T \mathbf{B} \mathbf{w}_i = 1$. We then have:

$$r(\mathbf{w}) = \frac{\sum_i c_i^2 \lambda_i}{\sum_i c_i^2}.$$

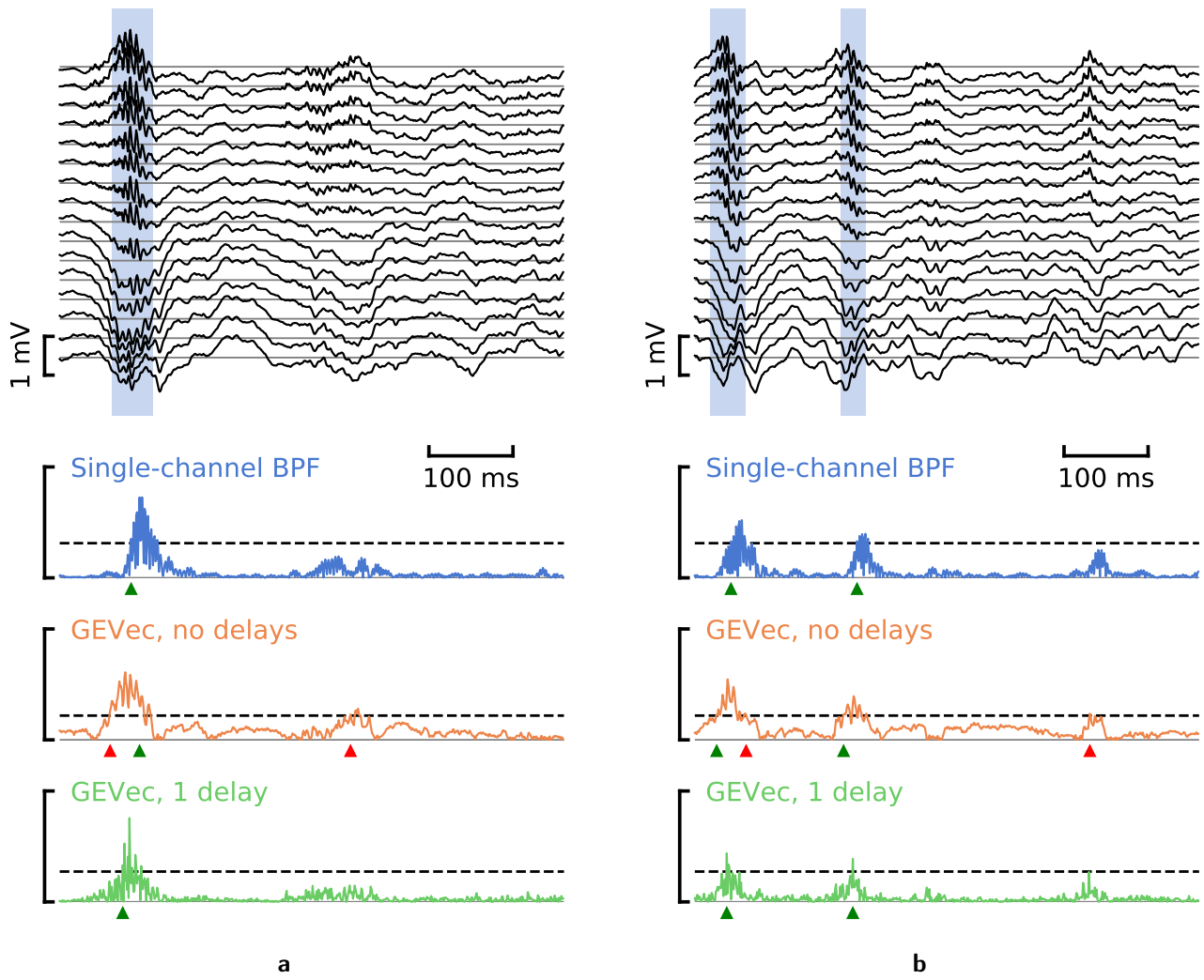
Each generalised Rayleigh quotient is thus a convex combination of generalised eigenvalues λ_i . The maximum of a convex combination of one-dimensional points is obtained in the largest of these points. If λ_1 is thus the largest generalised eigenvalue of (\mathbf{A}, \mathbf{B}) , then $\max r(\mathbf{w}) = \lambda_1$.

We have thus shown that $\arg \max r(\mathbf{w}) = \mathbf{w}_1$, where \mathbf{w}_1 is an eigenvector of (\mathbf{A}, \mathbf{B}) , and that its corresponding eigenvalue $\lambda_1 = \max r(\mathbf{w})$ is the largest of the eigenvalues of (\mathbf{A}, \mathbf{B}) .

□

Appendix C

Supplemental figures



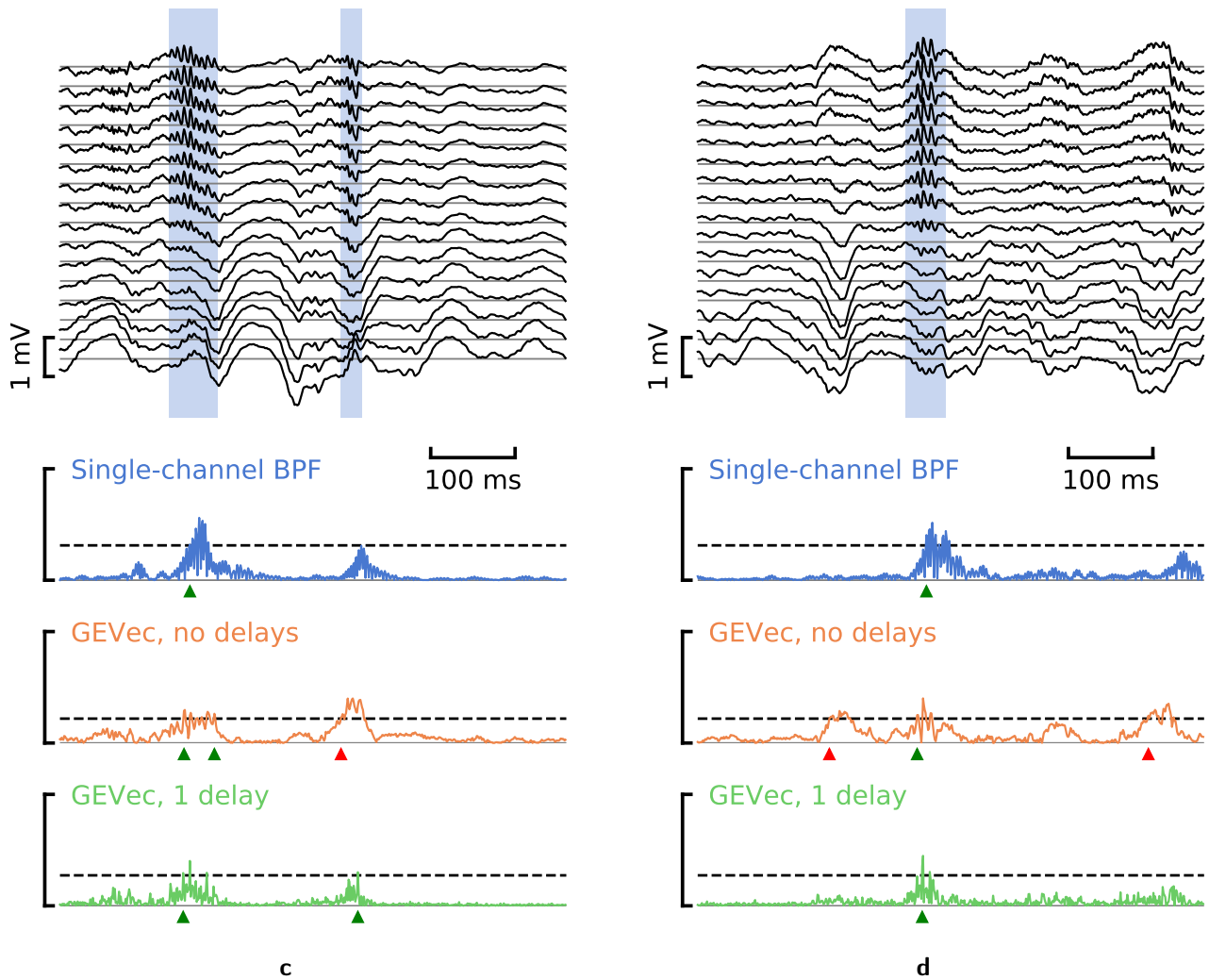


Figure C.1: Extracts from input data and corresponding linear filter output envelopes. See fig. 3.2 for legend.